J. Fluid Mech. (1994), *vol.* 271, *pp.* 285–309

Numerical simulations of particulate suspensions via a discretized Boltzmann equation. Part 1. Theoretical foundation

By ANTHONY J. C. LADD

Lawrence Livermore National Laboratory, Livermore, CA 94550, USA

(Received 6 July 1993 and in revised form 31 January 1994)

A new and very general technique for simulating solid–fluid suspensions is described; its most important feature is that the computational cost scales linearly with the number of particles. The method combines Newtonian dynamics of the solid particles with a discretized Boltzmann equation for the fluid phase; the many-body hydrodynamic interactions are fully accounted for, both in the creeping-flow regime and at higher Reynolds numbers. Brownian motion of the solid particles arises spontaneously from stochastic fluctuations in the fluid stress tensor, rather than from random forces or displacements applied directly to the particles. In this paper, the theoretical foundations of the technique are laid out, illustrated by simple analytical and numerical examples; in a companion paper (Part 2), extensive numerical tests of the method, for stationary flows, time-dependent flows, and finite-Reynolds-number flows, are reported.

1. Introduction

Numerical simulations, which take explicit account of the hydrodynamic forces between the suspended particles, are becoming useful tools for studying the dynamical and rheological properties of suspensions. There are at least three important flow regimes which can be addressed by numerical simulation: colloidal suspensions of sub-micron-sized particles, where Brownian forces and viscous forces balance; suspensions of macroscopic particles (i.e. larger than 10 μm), where the viscous forces alone are important; and flows at small but non-zero Reynolds number ($1 < Re < 100$). At present, computational cost is the limiting factor; even with supercomputers, it is not feasible to simulate more than about 100 particles with current methods. Thus, development of reliable and more efficient simulation techniques, able to cope with thousands of suspended particles, would have a significant impact on our understanding of particulate suspensions, complementing present experimental and theoretical knowledge. In this paper and a companion paper (Part 2, Ladd 1994) a new simulation technique for particulate suspensions is described; it combines Newtonian dynamics of the solid particles with a discretized Boltzmann model (McNamara & Zanetti 1988; Higuera, Succi & Benzi 1989) for the fluid. The basic idea is illustrated in figure 1, which shows five solid particles suspended in a background fluid. The fluid can be modelled as a continuum (figure 1*a*), as a molecular liquid (figure 1*b*), or as a discrete-velocity (lattice) gas (figure 1*c*). Because of the large scale separations, the dynamics of the solid particles are largely independent of the detailed mechanics of the suspending fluid. Discrete-velocity models of the fluid combine most of the features of a fully molecular simulation of solid and liquid phases, but are orders of magnitude

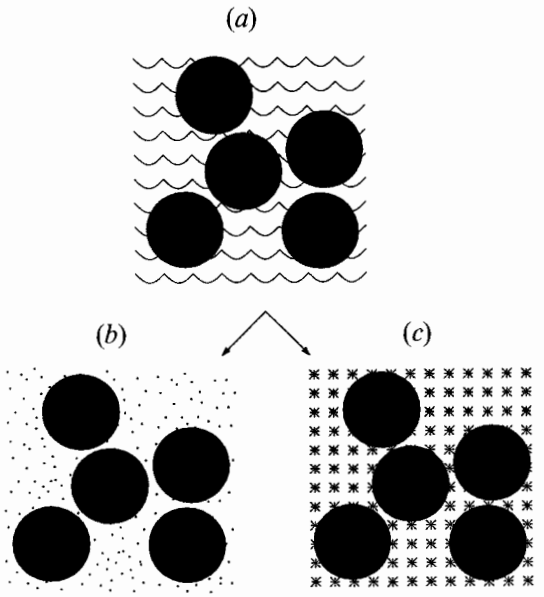

FIGURE 1. Microscopic models of a colloidal suspension. The dynamical properties of the large particles are insensitive to the detailed motions of the background fluid, so that the continuum fluid in (*a*) can be equally well replaced by either a molecular solvent (*b*) or a lattice gas (*c*). Lattice-gas/lattice-Boltzmann simulations are many orders of magnitude faster computationally.

faster computationally. They have many advantages over conventional methods of simulating particulate suspensions, which are usually based on complicated, computationally intensive solutions of the Stokes equations. By contrast, lattice-gas/lattice-Boltzmann simulations are fast, flexible, and simple. The new method is closely related to earlier suspension modelling using lattice-gas cellular automata (Ladd, Colvin & Frenkel 1988; Ladd & Frenkel 1989, 1990; Ladd, 1991; van der Hoef, Frenkel & Ladd 1991), but the large and uncontrollable statistical fluctuations present in lattice-gas models are suppressed, reducing the need for computationally expensive ensemble averaging.

In the classical theory of suspensions (Happel & Brenner 1986), the hydrodynamic interactions are assumed to be fully developed; in other words, there is a complete separation of timescales between the dynamics of the fluid and the motion of the solid particles. Most simulation methods (for instance Ermak & McCammon 1978; Brady & Bossis 1988; Ladd 1988; Tran-Cong & Phan-Thien 1989; Karrila, Fuentes & Kim 1989) utilize this approximation, even though it imposes a crippling numerical burden, associated with the *global* nature of the interactions; in such cases one must either make drastic simplifications (as in Ermak & McCammon 1978), or pay the steep computational cost of an algorithm that scales as at least the square and often as the cube of the number of particles (Brady & Bossis 1988; Ladd 1988; Tran-Cong & Phan-Thien 1989; Karrila *et al.* 1989).

The exact scaling depends on the problem to be solved. In some instances, particle velocities are computed for a given set of forces, in which case the computation can scale as N^2. However in many cases, for instance to simulate Brownian motion (Bossis & Brady 1987), the full $6N \times 6N$ diffusion coefficient matrix is needed; here the computational cost is of order N^3. Moreover, determining lubrication forces (Durlofsky, Brady & Bossis 1987) also involves an order-N^3 calculation of the friction coefficient matrix.

The Stokes equations can be solved very efficiently by spectral methods (Fogelson & Peskin 1988; Sulsky & Brackbill 1991). However, there are then the usual difficulties associated with incorporating solid boundary conditions into spectral codes; in the referenced work the particle surfaces are represented by point forces. Numerical studies of the Navier–Stokes equations indicate that, even for pure fluid flows, the lattice-Boltzmann equation is quite competitive with the best spectral methods (Chen *et al.* 1992).

In reality, hydrodynamic interactions develop in time and space from purely *local* forces generated at the solid–fluid surfaces, which then diffuse throughout the fluid. The Reynolds number introduces an effective range for the hydrodynamic interactions, proportional to $R_e^{-\frac{1}{2}}$. By contrast, truncating the creeping-flow hydrodynamic interactions beyond some critical distance is unlikely to be feasible; in analogous simulations of charged particles, spherical truncation of the Coulomb interaction between ions leads to large errors (Allen & Tildesley 1987). Recently a new simulation technique for particulate suspensions has been developed (Ladd 1993) which exploits the spatial locality of time-dependent hydrodynamic interactions; as a result the computational cost scales linearly with the number of particles. The method is also very flexible; the particle size and shape, the electrostatic interactions, the flow geometry, the Péclet number (the ratio of viscous forces to Brownian forces), and the Reynolds number (the ratio of inertial forces to viscous forces), can all be varied independently.

The popularity of boundary-integral methods, despite their obvious computational drawbacks, is a reflection of the difficulties involved in solving the Navier–Stokes equations in complex geometries. The drawbacks of an elementary finite-difference method, using a regular mesh, are discussed in §3.5 of Part 2. More complex finite-difference and finite-element techniques must deal with the challenge of finding a suitable computational mesh on which to calculate the fluid flow. In these two papers it will be shown that an algorithm based on a discretized Boltzmann equation can successfully solve complex fluid flow problems using only a simple cubic array of nodes.

Our computational method is based on the well-established connection between the dynamics of a dilute gas and the Navier–Stokes equations (Chapman & Cowling 1960). Thus, the problem is to determine the time evolution of the one-particle velocity distribution function $n(\boldsymbol{r}, \boldsymbol{v}, t)$, which defines the density of particles with velocity $\boldsymbol{v}$ around the space–time point $(\boldsymbol{r}, t)$. By introducing the assumption of molecular chaos, i.e. that successive binary collisions in a dilute gas are uncorrelated, Boltzmann was able to derive the integro-differential equation for n named after him (see Chapman & Cowling 1960):

$$\partial_t n + \boldsymbol{v}\cdot\nabla n = \left(\frac{\mathrm{d}n}{\mathrm{d}t}\right)_{coll}. \tag{1.1}$$

The Boltzmann equation has the form of a continuity equation for the velocity distribution function, with the addition of sources and sinks due to intermolecular collisions. The hydrodynamic fields, mass density ρ and momentum density $\boldsymbol{j} = \rho\boldsymbol{u}$, together with the momentum flux $\boldsymbol{\Pi}$, can be described by appropriate moments of n:

$$\left.\begin{aligned} \rho(\boldsymbol{r}, t) &= \int mn(\boldsymbol{r}, \boldsymbol{v}, t)\,\mathrm{d}\boldsymbol{v}, \\ \boldsymbol{j}(\boldsymbol{r}, t) &= \int (m\boldsymbol{v})\, n(\boldsymbol{r}, \boldsymbol{v}, t)\,\mathrm{d}\boldsymbol{v}, \\ \boldsymbol{\Pi}(\boldsymbol{r}, t) &= \int (m\boldsymbol{v}\boldsymbol{v})\, n(\boldsymbol{r}, \boldsymbol{v}, t)\,\mathrm{d}\boldsymbol{v}, \end{aligned}\right\} \tag{1.2}$$

where m is the molecular mass. In what follows, only the transport of mass and momentum will be considered; similar results can be derived for energy transport although the analysis is considerably more involved. (Ignoring energy conservation leads to the isothermal expression for the sound speed $c_s = (k_B T/m)^{\frac{1}{2}}$, rather than the adiabatic result $c_s = (5k_B T/3m)^{\frac{1}{2}}$. This is of no consequence to the later parts of this paper where the sound speed is treated as a variable parameter.)

Since intermolecular collisions are relatively rare in a dilute gas, the collisional contributions to the fluxes can be ignored; thus taking moments of (1.1) we find the expected conservation equations for mass and momentum,

$$\partial_t \rho + \nabla \cdot \boldsymbol{j} = 0, \quad \partial_t \boldsymbol{j} + \nabla \cdot \boldsymbol{\Pi} = 0. \tag{1.3}$$

The right-hand sides of (1.3) vanish because mass and momentum are conserved in the collision process, but finding a soluble equation for the momentum flux requires a more detailed consideration of the collision operator.

The difficulties associated with solving the Boltzmann equation arise from the complexity of the collision operator, written simply as $(\mathrm{d}n/\mathrm{d}t)_{coll}$ in (1.1). The earlier kinetic theory of Maxwell leads to a simplified form for the collision operator

$$\left(\frac{\mathrm{d}n}{\mathrm{d}t}\right)_{coll} = -\frac{n - n^{eq}}{\tau}, \tag{1.4}$$

where the relaxation time τ is an empirical parameter (which can be explicitly related to the rather unusual case of an r^{-5} intermolecular force law), and n^{eq} is the equilibrium Maxwell–Boltzmann distribution. Maxwell was able to show that the distribution

$$n^{eq} = \frac{\rho}{m}\left(\frac{m}{2\pi k_B T}\right)^{\frac{3}{2}} \exp\left(\frac{-m(\boldsymbol{v}-\boldsymbol{u})\cdot(\boldsymbol{v}-\boldsymbol{u})}{2k_B T}\right) \tag{1.5}$$

is a collisional invariant, i.e. $(\mathrm{d}n^{eq}/\mathrm{d}t)_{coll} = 0$. Thus, if the system should once reach such a uniform state, it would remain there indefinitely. Boltzmann's H-theorem showed that any initial distribution proceeds monotonically to n^{eq}, thus establishing it as the true equilibrium distribution for an ideal gas.

The Maxwell form for the collision operator is inadequate in some respects; it predicts a fixed ratio between the viscosity and thermal conductivity, and a vanishing coefficient of thermal diffusion. Boltzmann showed that these discrepancies could be removed by a detailed consideration of the effects of intermolecular forces on the collision process. Nevertheless, (1.4) is sufficient to give a simple and more-or-less correct understanding of the connection between the Boltzmann kinetic equation and Navier–Stokes fluid dynamics. The distribution function is written as a sum of equilibrium and non-equilibrium terms

$$n = n^{eq} + n^{neq}, \tag{1.6}$$

where the non-equilibrium distribution, n^{neq}, has the important property that its zeroth and first velocity moments vanish (cf. (1.2)), along with the trace of the second moment $\int (mv^2)\, n^{neq}(\boldsymbol{r}, \boldsymbol{v}, t)\, \mathrm{d}\boldsymbol{v}$. The momentum flux can be similarly decomposed; its equilibrium contribution can be evaluated directly from (1.5),

$$\boldsymbol{\Pi}^{eq} = \frac{\rho k_B T}{m} \boldsymbol{1} + \rho \boldsymbol{u}\boldsymbol{u}, \tag{1.7}$$

and is equivalent to the Eulerian form for the momentum flux, with an ideal-gas equation of state $p = \rho k_B T/m$. The non-equilibrium momentum flux $\overline{\boldsymbol{\Pi}}^{neq}$ (the overbar

indicates the traceless projection) can be obtained from a kinetic equation for $\boldsymbol{\Pi}$ analogous to (1.3),

$$\partial_t \overline{\boldsymbol{\Pi}}^{eq} + \int (m\overline{\boldsymbol{v}\boldsymbol{v}}\boldsymbol{v}) \cdot \boldsymbol{\nabla} n^{eq}(\boldsymbol{r}, \boldsymbol{v}, t)\, \mathrm{d}\boldsymbol{v} = (-\tau^{-1})\, \overline{\boldsymbol{\Pi}}^{neq}. \tag{1.8}$$

In deriving (1.8) it has been assumed that the system is close to equilibrium, so that n can be replaced by n^{eq}, and that the hydrodynamic timescales are large compared with τ. The left-hand side of (1.8) can be evaluated explicitly, using (1.5) and (1.7); the result is

$$\overline{\boldsymbol{\Pi}}^{neq} = -\frac{\rho k_B T \tau}{m} (\overline{\boldsymbol{\nabla} \boldsymbol{u}} + \overline{\boldsymbol{\nabla} \boldsymbol{u}}^t), \tag{1.9}$$

which is the Navier–Stokes form for the viscous momentum flux with viscosity $\eta = \rho k_B T \tau / m$.

In the preceding discussion it was shown, in a rather approximate fashion, that the Navier–Stokes equations follow directly from the Boltzmann equation in the limit that the dimensions of the macroscopic flow fields are much larger than the mean free path between molecular collisions; a rigorous derivation of this result can be found in Chapman & Cowling (1960). Because of its complexity, there are few direct numerical solutions of the Boltzmann equation (an exception is Yen 1984), but stochastic, particle-based simulations are quite commonly used in molecular gasdynamics; the merits of this approach are discussed in Bird (1976, 1990). A variant of this approach has recently been introduced to simulate particle suspensions (Hoogerbrugge & Koelman 1992; Koelman & Hoogerbrugge 1993). However, a key realization is that the one-particle distribution function $n(\boldsymbol{r}, \boldsymbol{v}, t)$ contains much more information than is strictly necessary to solve fluid-dynamics problems. Hence in recent years, there has been a resurgence of interest in discrete-velocity or lattice-gas models (Frisch, Hasslacher & Pomeau 1986; Frisch *et al.* 1987), in which the continuous distribution of molecular velocities is replaced by a few discrete values, carefully chosen to ensure that the moment equations (1.3), (1.7), and (1.9) are reproduced correctly. Numerical studies have shown that lattice-Boltzmann simulations are comparable in accuracy and computational cost to state-of-the-art Navier–Stokes solvers, either finite difference (McNamara & Alder 1993) or spectral (Chen *et al.* 1992).

In the lattice-Boltzmann approximation, the fundamental quantity is the discretized one-particle velocity distribution function $n_i(\boldsymbol{r}, t)$, which describes the number of particles at a particular node of the lattice $\boldsymbol{r}$, at a time t, with a velocity $\boldsymbol{c}_i$; $\boldsymbol{r}$, t, and $\boldsymbol{c}_i$ are discrete, whereas n_i is continuous. As before, the hydrodynamic fields, ρ, $\boldsymbol{j}$, and $\boldsymbol{\Pi}$, are moments of this discrete velocity distribution (cf. (1.2)):

$$\rho = \sum_i n_i, \quad \boldsymbol{j} = \sum_i n_i \boldsymbol{c}_i, \quad \boldsymbol{\Pi} = \sum_i n_i \boldsymbol{c}_i \boldsymbol{c}_i. \tag{1.10}$$

The lattice-Boltzmann equation has two important properties which are valuable for simulations of particulate suspensions. First, the connection to molecular mechanics makes it possible to derive simple local rules for the interactions between the fluid and the suspended solid particles (Ladd 1993); this was demonstrated in our earlier lattice-gas simulations (Ladd & Frenkel 1990; Ladd 1991; van der Hoef *et al.* 1991). Second, the discrete one-particle distribution function n_i contains additional information about the dynamics of the fluid beyond that contained in the Navier–Stokes equations; in particular, the fluid stress tensor, although dynamically coupled to the velocity gradient (Frisch *et al.* 1987), has an independent significance at short times. This

additional flexibility allows us to simulate molecular fluctuations, leading to Brownian motion of the suspended particles. To do this, a random fluctuation, uncorrelated in space and time, is added to the fluid stress tensor (Ladd 1993); the variance of the fluctuations defines the effective temperature of the fluctuating fluid (Landau & Lifshitz 1959). This approach is quite different from Brownian dynamics (Ermak & McCammon 1978) or Stokesian dynamics (Bossis & Brady 1987), where random fluctuations are applied directly to the particles; to include hydrodynamic interactions in these methods requires sampling from the $6N \times 6N$ diffusion matrix, which is extremely time consuming.

The layout of the remainder of this paper is as follows. In §2 the lattice-Boltzmann model is described and its connection to Navier–Stokes fluid dynamics established. Section 3 describes the implementation of the solid–fluid boundary conditions at the microscopic level, together with analytic and numerical results for shear flows and channel flows. Fluctuations are introduced in §4; it is verified that the simulations satisfy the fluctuation-dissipation theorem and that the correct shear viscosity can be obtained from an appropriate Green–Kubo formula. In the companion paper (Ladd 1994, referred to hereafter as Part 2), results of extensive tests of creeping-flow hydrodynamics are reported, for both periodic arrays and random distributions of spheres; time-dependent and finite-Reynolds-number flows are also discussed. Three-dimensional simulations of up to 1024 colloidal particles, moving under the action of Brownian forces, are also reported.

2. Discrete Boltzmann approximation

The computational utility of the lattice-Boltzmann equation is related to the realization that only a small set of discrete velocities is necessary to simulate the Navier–Stokes equations (Frisch *et al.* 1986). It may be helpful in what follows to imagine an underlying mechanical model in which identical particles move with discrete velocities from node to node of a regular lattice; much of the kinetic theory of dilute gases, outlined in §1, can then be carried over directly to the discretized version. The specific model used in this work has 18 different velocities corresponding to the near-neighbour and second-neighbour directions of a simple cubic lattice. Thus there are six velocities of speed 1, corresponding to (100) directions in the lattice, and 12 velocities of speed $\sqrt{2}$, corresponding to the (110) directions, for a total of 18. All quantities in this paper are expressed in 'lattice units', for which the distance between nearest-neighbour nodes and the time for the particles to travel from node to node are both unity. Note that the velocities are such that all particles move from node to node simultaneously.

The time evolution of the distribution functions n_i is described by a discrete analogue of the Boltzmann equation (Frisch *et al.* 1987),

$$n_i(\boldsymbol{r}+\boldsymbol{c}_i, t+1) = n_i(\boldsymbol{r}, t)+\Delta_i(\boldsymbol{r}, t), \tag{2.1}$$

where Δ_i is the change in n_i due to instantaneous molecular collisions at the lattice nodes. The post-collision distribution $n_i+\Delta_i$ is propagated for one time step, in the direction $\boldsymbol{c}_i$. The collision operator $\Delta(n)$ depends on all the n_i at the node, denoted collectively by $n(\boldsymbol{r}; t)$; it can take any form, subject to the constraints of mass and momentum conservation. An exact expression for the Boltzmann collision operator has been derived for several different lattice-gas models (Frisch *et al.* 1987; McNamara & Zanetti 1988), under the usual assumption that the distribution functions $n(\boldsymbol{r}; t)$ are uncorrelated from those at previous times. However, such collision operators are

complex and ill-suited to numerical simulation. A computationally useful form for the collision operator, similar to (1.4), can be constructed by linearizing the collision operator about the local equilibrium n^{eq} (Higuera *et al.* 1989), i.e.

$$\Delta_i(n) = \Delta_i(n^{eq}) + \sum_j \mathscr{L}_{ij}(n_j - n_j^{eq}), \tag{2.2}$$

where $\mathscr{L}$ is the linearized collision operator, and $\Delta_i(n^{eq}) = 0$ by definition. It is not necessary to construct a particular collision operator and from this calculate $\mathscr{L}$; rather it is sufficient to consider the general principles of conservation and symmetry and then to construct the eigenvalues and eigenvectors of $\mathscr{L}$. However, before doing this, the proper form for the equilibrium distribution function will be determined.

To establish the connection between molecular mechanics and fluid dynamics, it is again necessary to split the distribution function into an equilibrium part and a non-equilibrium part

$$n_i = n_i^{eq} + n_i^{neq}. \tag{2.3}$$

The equilibrium distribution is a collisional invariant (i.e. $\Delta_i(n^{eq}) = 0$), and depends only on the local hydrodynamic variables (mass density, stream velocity and, in some cases, energy density); for a molecular gas n^{eq} is the Maxwell–Boltzmann distribution, (1.5). It is well known that a Maxwell–Boltzmann local equilibrium leads to the Euler equations of hydrodynamics ((1.3) and (1.7)); however the most-probable (equilibrium) distribution functions of discrete-velocity lattice gases give rise to density-dependent advection velocities and velocity-dependent pressures (Frisch *et al.* 1987). Therefore we seek a constrained equilibrium distribution for our discrete-velocity model that will lead to the correct macroscopic fluid dynamics at the Euler level; the required form for the moments of the velocity distribution function are

$$\rho = \sum_i n_i^{eq}, \quad \boldsymbol{j} = \sum_i n_i^{eq} \boldsymbol{c}_i, \quad \boldsymbol{\Pi}^{eq} = \sum_i n_i^{eq} \boldsymbol{c}_i \boldsymbol{c}_i = p\boldsymbol{1} + \rho \boldsymbol{u}\boldsymbol{u}, \tag{2.4}$$

where p is the pressure and $\boldsymbol{\Pi}^{eq}$ is the non-dissipative part of the momentum flux. As in the usual kinetic theory of gases, the viscous fluxes come from the non-equilibrium part of the distribution function.

The equilibrium distribution can be expressed as a series expansion in powers of the flow velocity $\boldsymbol{u}$,

$$n_i^{eq} = \rho[a_0^{c_i} + a_1^{c_i} \boldsymbol{u}\cdot\boldsymbol{c}_i + a_2^{c_i} \overline{\boldsymbol{u}\boldsymbol{u}} : \overline{\boldsymbol{c}_i \boldsymbol{c}_i} + a_3^{c_i} u^2], \tag{2.5}$$

where $\overline{\boldsymbol{u}\boldsymbol{u}} = \boldsymbol{u}\boldsymbol{u} - \frac{1}{3}u^2\boldsymbol{1}$ is the traceless part of $\boldsymbol{u}\boldsymbol{u}$; (2.5) has the same functional form as a small-u expansion of the Maxwell–Boltzmann distribution function. The moments of the distribution function, (2.4), can be expressed in terms of the coefficients $a_n^{c_i}$, which are functions only of the speed, c_i:

$$\rho^{-1} \sum_i n_i^{eq} = 6a_0^1 + 12a_0^{\sqrt{2}} + [6a_3^1 + 12a_3^{\sqrt{2}}] u^2, \tag{2.6}$$

$$\rho^{-1} \sum_i n_i^{eq} c_{i\alpha} = [2a_1^1 + 8a_1^{\sqrt{2}}] u_\alpha, \tag{2.7}$$

$$\rho^{-1} \sum_i n_i^{eq} c_i^2 = 6a_0^1 + 24a_0^{\sqrt{2}} + [6a_3^1 + 24a_3^{\sqrt{2}}] u^2, \tag{2.8}$$

$$\rho^{-1} \sum_i n_i^{eq} \overline{c_{i\alpha} c_{i\beta}} = \{2a_2^1[\delta_{\alpha\beta\gamma\delta} - \tfrac{1}{3}\delta_{\alpha\beta}\delta_{\gamma\delta}] + 4a_2^{\sqrt{2}}[-\delta_{\alpha\beta\gamma\delta} - \tfrac{1}{3}\delta_{\alpha\beta}\delta_{\gamma\delta} + \delta_{\alpha\gamma}\delta_{\beta\delta} + \delta_{\alpha\delta}\delta_{\beta\gamma}]\} \overline{u_\gamma u_\delta}, \tag{2.9}$$

$$\rho^{-1}\sum_i n_i^{eq} c_{i\alpha} c_{i\beta} c_{i\gamma} = \{2a_1^1 \delta_{\alpha\beta\gamma\delta} + 4a_1^{1/2}[-\delta_{\alpha\beta\gamma\delta} + \delta_{\alpha\beta}\delta_{\gamma\delta} + \delta_{\alpha\gamma}\delta_{\beta\delta} + \delta_{\alpha\delta}\delta_{\beta\gamma}]\} u_\delta. \tag{2.10}$$

The tensor $\delta_{\alpha\beta\gamma\delta}$ is unity when all the subscripts are the same (i.e. $\delta_{xxxx} = \delta_{yyyy} = \delta_{zzzz} = 1$) and zero otherwise; $\delta_{\alpha\beta}$ is the Kronecker delta. The third-order moments, (2.10), do not contribute to the Euler equations, but they do contribute to the viscous stresses because of the second-order Chapman–Enskog expansion (see (2.28)). Thus they must be proportional to the fourth-rank identity tensor $(\delta_{\alpha\beta}\delta_{\gamma\delta} + \delta_{\alpha\gamma}\delta_{\beta\delta} + \delta_{\alpha\delta}\delta_{\beta\gamma})$; otherwise the viscous part of the momentum flux will not be isotropic. A comparison of (2.6)–(2.9) with (2.4), together with the isotropy condition in (2.10), is sufficient to determine all the coefficients:

$$\left.\begin{aligned} a_0^1 = \tfrac{1}{6}(2-3c_s^2), \quad a_1^1 = \tfrac{1}{6}, \quad a_2^1 = \tfrac{1}{4}, \quad a_3^1 = -\tfrac{1}{6}, \\ a_0^{1/2} = \tfrac{1}{12}(3c_s^2-1), \quad a_1^{1/2} = \tfrac{1}{12}, \quad a_2^{1/2} = \tfrac{1}{8}, \quad a_3^{1/2} = \tfrac{1}{12}. \end{aligned}\right\} \tag{2.11}$$

The definition of the pressure (2.4) indicates that it is proportional to the density, i.e. $p = \frac{1}{3}(\sum_i n_i^{eq} c_i^2 - \rho u^2) = \rho c_s^2$; later it will be shown that c_s is the speed of sound (see (2.26)), as in a normal gas. Since the distribution function must always be positive, the speed of sound is bounded by the limits $\frac{1}{3} \leqslant c_s^2 \leqslant \frac{2}{3}$. However, as the sound speed approaches either of the two limits, the simulation becomes unstable with respect to variations in fluid velocity. In our simulations, the intermediate value $c_s^2 = \frac{1}{2}$ is used, to maximize the stability with respect to variations in flow velocity; in this case

$$a_0^1 = \tfrac{1}{12}, \quad a_0^{1/2} = \tfrac{1}{24}. \tag{2.12}$$

Having constructed an equilibrium distribution appropriate for the inviscid (Euler) equations, let us next consider how to obtain the correct form for the viscous terms in the fluid equations. We require that the linearized collision operator satisfy the following eigenvalue equations:

$$\sum_i \mathscr{L}_{ij} = 0, \quad \sum_i \boldsymbol{c}_i \mathscr{L}_{ij} = 0, \quad \sum_i \overline{\boldsymbol{c}_i \boldsymbol{c}_i} \mathscr{L}_{ij} = \lambda \overline{\boldsymbol{c}_j \boldsymbol{c}_j}, \quad \sum_i c_i^2 \mathscr{L}_{ij} = \lambda_B c_j^2. \tag{2.13}$$

The first two equations follow from conservation of mass and momentum and the last two equations describes the isotropic relaxation of the stress tensor; the eigenvalues λ and λ_B are related to the shear and bulk viscosities (2.34). Equations (2.13) account for 10 of the 18 eigenvectors of $\mathscr{L}$. The remaining eight modes, comprising some higher-order moments of $\mathscr{L}$, are not relevant to simulations of the Navier–Stokes equations and will be ignored. Their eigenvalues are set to -1 so that these modes are then projected out entirely from the post-collision distribution; this both simplifies the simulation and ensures the fastest possible relaxation of the non-hydrodynamic modes. The computational procedure to update the lattice-Boltzmann equation is therefore quite straightforward. At each site the moments ρ, $\boldsymbol{j}$, and $\boldsymbol{\Pi}$ (1.10), and the equilibrium momentum flux $\boldsymbol{\Pi}^{eq}$, (2.4), are calculated; the momentum flux is then updated according to (2.13):

$$\Pi'_{\alpha\beta} = \Pi^{eq}_{\alpha\beta} + (1+\lambda)(\overline{\Pi}_{\alpha\beta} - \overline{\Pi}^{eq}_{\alpha\beta}) + \tfrac{1}{3}(1+\lambda_B)(\Pi_{\gamma\gamma} - \Pi^{eq}_{\gamma\gamma})\,\delta_{\alpha\beta}. \tag{2.14}$$

The post-collision distribution, $n_i + \Delta_i(n)$, is determined by the requirement that the new populations are consistent with (1.10), so that

$$n_i + \Delta_i(n) = a_0^{c_i}\rho + a_1^{c_i} j_\alpha c_{i\alpha} + a_2^{c_i} \Pi'_{\alpha\beta} \overline{c_{i\alpha} c_{i\beta}} + a_3^{c_i}(\Pi'_{\alpha\alpha} - 3\rho c_s^2); \tag{2.15}$$

the term $-3\rho c_s^2 a_3^{c_i}$ keeps $\boldsymbol{\Pi}'$ orthogonal to ρ.

Next we examine the macrodynamical behaviour arising from the lattice-Boltzmann equation; our method of solution is the usual multi-timescale analysis (Frisch *et al.* 1987). We begin with conservation equations for the moments of the distribution function:

$$\sum_i n_i(\boldsymbol{r}+\boldsymbol{c}_i, t+1) = \sum_i n_i(\boldsymbol{r}, t), \tag{2.16}$$

$$\sum_i n_i(\boldsymbol{r}+\boldsymbol{c}_i, t+1)\, c_{i\alpha} = \sum_i n_i(\boldsymbol{r}, t)\, c_{i\alpha}, \tag{2.17}$$

$$\sum_i n_i(\boldsymbol{r}+\boldsymbol{c}_i, t+1)\, \overline{c_{i\alpha} c_{i\beta}} = \sum_i n_i(\boldsymbol{r}, t)\, \overline{c_{i\alpha} c_{i\beta}} + \lambda \sum_i n_i^{neq}(\boldsymbol{r}, t)\, \overline{c_{i\alpha} c_{i\beta}}, \tag{2.18}$$

$$\sum_i n_i(\boldsymbol{r}+\boldsymbol{c}_i, t+1)\, c_i^2 = \sum_i n_i(\boldsymbol{r}, t)\, c_i^2 + \lambda_B \sum_i n_i^{neq}(\boldsymbol{r}, t)\, c_i^2. \tag{2.19}$$

To find the long-time long-wavelength dynamics, a scaling parameter ϵ is introduced, defined as the ratio of the lattice spacing to a characteristic macroscopic length; the hydrodynamic limit corresponds to $\epsilon \ll 1$. In a molecular gas the appropriate scaling parameter is the Knudsen number, the ratio of the mean-free path between collisions to the macroscopic lengthscale. The parameter ϵ plays a similar role to the Knudsen number in the Chapman–Enskog method (Chapman & Cowling 1960); it is used, first of all, to separate the relaxation of the equilibrium and non-equilibrium distributions (cf. (2.3)),

$$n_i = n_i^{eq} + \epsilon n_i^{neq}. \tag{2.20}$$

However, because the lattice spacing and the mean-free path are comparable, there are additional contributions to the viscous momentum flux, which do not appear in the ordinary kinetic theory of gases (see (2.32)). In order to remove discrete lattice artifacts from the macroscopic equations, it is convenient to define a macroscopic space scale $\boldsymbol{r}_1 = \epsilon \boldsymbol{r}$, and two macroscopic timescales $t_1 = \epsilon t$ and $t_2 = \epsilon^2 t$; this enables a separation to be made between the propagation of sound (t_1) and the diffusion of vorticity (t_2) (Frisch *et al.* 1987).

Expanding the finite differences, $n_i(\boldsymbol{r}+\boldsymbol{c}_i, t+1) - n_i(\boldsymbol{r}, t)$ ((2.16)–(2.19)), to second order about $\boldsymbol{r}$ and t, and collecting terms that are first order in ϵ we obtain the relaxation on the t_1 timescale:

$$\partial_{t_1} \sum_i n_i^{eq} + \nabla_\alpha \sum_i n_i^{eq} c_{i\alpha} = 0, \tag{2.21}$$

$$\partial_{t_1} \sum_i n_i^{eq} c_{i\alpha} + \nabla_\beta \sum_i n_i^{eq} c_{i\alpha} c_{i\beta} = 0, \tag{2.22}$$

$$\partial_{t_1} \sum_i n_i^{eq} c_{i\alpha} c_{i\beta} + \nabla_\gamma \sum_i n_i^{eq} c_{i\alpha} c_{i\beta} c_{i\gamma} = \lambda \sum_i n_i^{neq} \overline{c_{i\alpha} c_{i\beta}} + \tfrac{1}{3}\lambda_B \sum_i n_i^{neq} c_i^2 \delta_{\alpha\beta}. \tag{2.23}$$

The gradient operator refers to derivatives on the macroscopic $\boldsymbol{r}_1$ space scale, i.e. $\boldsymbol{\nabla} \equiv \partial_{\boldsymbol{r}_1}$. The equations for mass and momentum conservation ((2.21) and (2.22)) can be rewritten using (2.4):

$$\partial_{t_1} \rho + \boldsymbol{\nabla} \cdot (\rho \boldsymbol{u}) = 0, \tag{2.24}$$

$$\partial_{t_1} (\rho \boldsymbol{u}) + \boldsymbol{\nabla} \cdot (p\boldsymbol{1} + \rho \boldsymbol{u}\boldsymbol{u}) = 0, \tag{2.25}$$

which are the Euler equations of hydrodynamics. Substituting the equation of state $p = \rho c_s^2$ and linearizing the Euler equations with respect to $\delta\rho$ and $\boldsymbol{u}$, it is found that, for small density fluctuations,

$$\partial_{t_1}^2 \rho = c_s^2 \nabla^2 \rho. \tag{2.26}$$

Equation (2.26) shows that density fluctuations relax via the propagation of sound waves, on a timescale t_1, and therefore decouple from the t_2 timescale evolution of the viscous stresses. The time derivative that appears in (2.23) can be evaluated by using (2.24) and (2.25) to express the time derivatives of ρ and $\rho\boldsymbol{u}$ in terms of spatial derivatives:

$$\partial_{t_1}\sum_i n_i^{eq} c_{i\alpha} c_{i\beta} = \partial_{t_1}(\rho c_s^2 \delta_{\alpha\beta} + \rho u_\alpha u_\beta)$$
$$= -\nabla_\gamma(\rho u_\alpha u_\beta u_\gamma) - c_s^2[u_\alpha \nabla_\beta \rho + u_\beta \nabla_\alpha \rho + \nabla_\gamma(\rho u_\gamma)\delta_{\alpha\beta}]. \quad (2.27)$$

The spatial derivative of the third-order moment can be evaluated directly from (2.10) and (2.11):

$$\nabla_\gamma \sum_i n^{eq} c_{i\alpha} c_{i\beta} c_{i\gamma} = \tfrac{1}{3}[\nabla_\alpha(\rho u_\beta) + \nabla_\beta(\rho u_\alpha) + \nabla_\gamma(\rho u_\gamma)\delta_{\alpha\beta}]. \quad (2.28)$$

In the incompressible limit, variations in density can be ignored, so that

$$\partial_{t_1}\sum_i n_i^{eq}\overline{c_{i\alpha}c_{i\beta}} + \nabla_\gamma \sum_i n_i^{eq}\overline{c_{i\alpha}c_{i\beta}}c_{i\gamma} = \tfrac{1}{3}\rho[\nabla_\alpha u_\beta + \nabla_\beta u_\alpha - \tfrac{2}{3}\nabla_\gamma u_\gamma \delta_{\alpha\beta}], \quad (2.29)$$

with errors of order ∇u^3. Then, from (2.23), the Navier–Stokes form for the viscous stresses can be obtained:

$$\sigma_{\alpha\beta} = -\sum_i n_i^{neq}\overline{c_{i\alpha}c_{i\beta}} = -(\rho/3\lambda)(\nabla_\alpha u_\beta + \nabla_\beta u_\alpha - \tfrac{2}{3}\nabla_\gamma u_\gamma \delta_{\alpha\beta}). \quad (2.30)$$

Hereafter the non-equilibrium (viscous) contributions to the pressure will be ignored. Since the Mach number in our simulations is typically 10^{-2} or less, the effects of compressibility can be safely ignored. It is interesting to note that if the speed of sound c_s were set to $\sqrt{\frac{1}{3}}$ instead of $\sqrt{\frac{1}{2}}$, then inspection of (2.27) and (2.28) indicates that the correct form for the viscous stresses, including the non-equilibrium pressure, would be obtained (with corrections of order ∇u^3), even for non-zero Mach numbers. For such simulations, an additional density of zero-velocity particles is required to maintain stability (McNamara & Alder 1993).

The t_2 relaxation of the mass and momentum densities can be found from the order-ϵ^2 terms in the expansion of (2.16) and (2.17):

$$\partial_{t_2}\sum_i n_i^{eq} = \partial_{t_2}\rho = 0, \quad (2.31)$$

$$\partial_{t_2}\sum_i n_i^{eq} c_{i\alpha} + \tfrac{1}{2}\nabla_\beta(\partial_{t_1}\sum_i n_i^{eq} c_{i\alpha}c_{i\beta} + \nabla_\gamma \sum_i n_i^{eq} c_{i\alpha}c_{i\beta}c_{i\gamma}) + \nabla_\beta \sum_i n_i^{neq} c_{i\alpha}c_{i\beta} = 0. \quad (2.32)$$

Equation (2.31) shows that the fluid is incompressible on the t_2 timescale; all relaxation of density fluctuations takes place on the t_1 timescale. Using (2.29) and (2.30) the long-time variation of the viscous stresses can be expressed in a form identical to the incompressible Navier–Stokes equations,

$$\partial_{t_2}(\rho\boldsymbol{u}) = \eta\nabla^2\boldsymbol{u}, \quad (2.33)$$

where

$$\eta = -\tfrac{1}{6}\rho(2/\lambda + 1) \quad (2.34)$$

is the shear viscosity; once again terms proportional to $\nabla\cdot\boldsymbol{u}$ are neglected.

The shear viscosity, (2.34), contains two distinct contributions: the first, proportional to λ^{-1}, arises from the molecular-like collisions, (2.13); the second term comes from the

diffusion of momentum caused by the finite lattice, (2.29). In most situations of practical interest the collisional and lattice contributions to the viscosity are of comparable magnitude. Fortunately they both have exactly the same dependence on velocity gradient, so that they may be combined into a single transport coefficient. A linear stability analysis shows that λ must be bounded in the range $-2 < \lambda < 0$ (Higuera *et al.* 1989; McNamara & Alder 1993), otherwise the shear stress grows exponentially in time and the simulation is unstable. The bounds on λ correspond to the simple physical requirement that the viscosity is positive. At non-zero Reynolds numbers the viscosity is bounded by a more stringent nonlinear stability criterion, which has not yet been worked out in detail, but whose general character is known. Essentially the quantity $\rho v^2/\eta$ (v is a characteristic flow velocity) must be smaller than some positive constant of order 1; thus there is an upper bound to the flow velocity, proportional to the square root of the viscosity.

Combining the relaxation of the momentum density on the t_1 and t_2 timescales leads to the incompressible Navier–Stokes equation

$$\partial_t(\rho \boldsymbol{u}) + \boldsymbol{\nabla}\cdot(\rho \boldsymbol{u}\boldsymbol{u}) = -\boldsymbol{\nabla} p + \eta \nabla^2 \boldsymbol{u}, \tag{2.35}$$

with equation of state $p = \rho c_s^2$. Once again we point out that for the 18 velocity model used in this work, the simulations are only valid at low Mach numbers; slightly more complex models are needed to capture compressibility effects correctly. In the remainder of this paper, it will be assumed that the simulations will be run under conditions of low Mach number, with particle velocities $\boldsymbol{U}$ much less than the sound speed c_s; thus $\boldsymbol{\nabla}\cdot\boldsymbol{u} = 0$ to a good approximation.

Many flows involving particulate suspensions occur at low Reynolds number, and can be modelled by the creeping-flow or Stokes equations

$$\boldsymbol{\nabla}\cdot\boldsymbol{u} = 0, \quad \boldsymbol{\nabla} p = \eta \nabla^2 \boldsymbol{u}; \tag{2.36}$$

or, in terms of the momentum density $\boldsymbol{j} = \rho \boldsymbol{u}$ and the kinematic viscosity $\nu = \eta/\rho$,

$$\boldsymbol{\nabla}\cdot\boldsymbol{j} = 0, \quad \boldsymbol{\nabla} p = \nu \nabla^2 \boldsymbol{j}. \tag{2.37}$$

In our simulations the Stokes equations are not modelled directly, but rather as a long-time limit of the linearized Navier–Stokes equations

$$\partial_t \rho = -\boldsymbol{\nabla}\cdot\boldsymbol{j}, \quad \partial_t \boldsymbol{j} = -\boldsymbol{\nabla} p + \nu \nabla^2 \boldsymbol{j}; \tag{2.38}$$

(2.38) can be simulated directly by a change in the equilibrium distribution (cf. (2.5)),

$$n_i^{eq} = a_0^{c_i}\rho + a_1^{c_i}\boldsymbol{j}\cdot\boldsymbol{c}_i. \tag{2.39}$$

Finally, a significant simplification of the code occurs when $\lambda = -1$, corresponding to a viscosity $\eta = \frac{1}{6}\rho$. Although such a large viscosity is not suitable for high-Reynolds-number flows, in the creeping flow limit it allows for a considerable simplification of the collision operator

$$n_i + \Delta_i(n) = a_0^{c_i}\rho + a_1^{c_i}\boldsymbol{j}\cdot\boldsymbol{c}_i, \tag{2.40}$$

which requires less than half the number of floating-point operations as (2.15); most of our $R_e = 0$ simulations use this viscosity.

3. Solid–fluid boundary conditions

To simulate the hydrodynamic interactions between solid particles in suspension, the lattice-Boltzmann model must be modified to incorporate the boundary conditions imposed on the fluid by the solid particles. The basic methodology is illustrated in

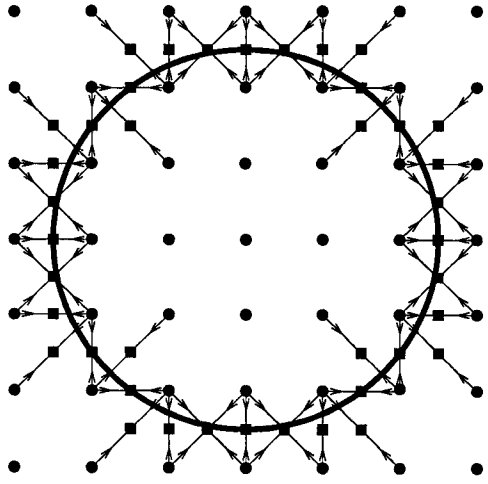

FIGURE 2. Location of the boundary nodes for a circular object of radius 2.5 lattice spacings. The velocities along links cutting the boundary surface are indicated by arrows. The locations of the boundary nodes are shown by solid squares and the lattice nodes by solid circles.

figure 2. The solid particles are defined by a boundary surface, which can be of any size or shape; in figure 2 it is a circle. When placed on the lattice, the boundary surface cuts some of the links between lattice nodes. The fluid particles moving along these links interact with the solid surface at boundary nodes placed halfway along the links. Thus a discrete representation of the particle surface is obtained, which becomes more and more precise as the particle gets larger.

Lattice nodes on either side of the boundary surface are treated in an identical fashion, so that fluid fills the whole volume of space, both inside and outside the solid particles. The boundary-node update rules described later in the section (see (3.2) and (3.3)) decouple the interior and exterior fluid regions, so fluctuations in the interior fluid have no effect on the exterior flow. The interior fluid is kept for computational convenience only, since it avoids the necessity of creating and destroying fluid as the particle moves. In the creeping-flow regime the interior fluid has relaxed to a rigid-body motion, characterized by the particle velocity and angular velocity, and exerts no force or torque on the particle. However, the interior fluid does exert a time-dependent force, which, to leading order in $a^2/\nu t$, is equivalent to its inertial mass. Further deviations at short times are discussed in §5 of Part 2; in general they are negligible.

In comparison with our previous work (Ladd *et al.* 1988; Ladd & Frenkel 1989, 1990; Ladd 1991; van der Hoef *et al.* 1991), here we have chosen to place the boundary nodes on the links connecting the interior and exterior regions, whereas in our lattice-gas simulations they were located on the nodes closest to the boundary surface. There is little to choose between the two methods; the link method has the advantage that it provides a somewhat higher resolution of the solid boundary surface, as can be seen (figure 2) from the much larger number of boundary nodes compared with the number of lattice nodes just inside the surface. On the other hand the node method is faster, although this is of less significance in the computationally more intensive lattice-Boltzmann (as opposed to lattice-gas) simulations. Although at present our lattice-Boltzmann simulations have been limited to simple symmetrical objects – spheres, disks and plane walls – this restriction is not fundamental: in fact a limited number of lattice-gas simulations containing elongated objects have already been reported (van der Hoef 1992).

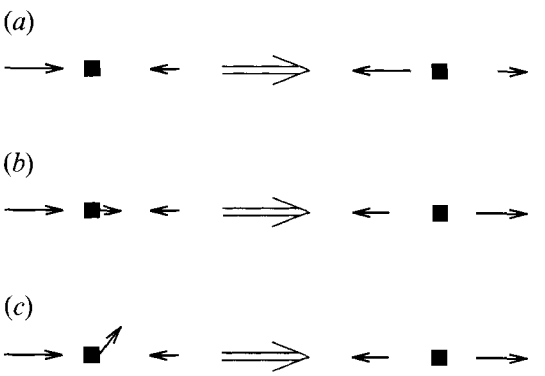

FIGURE 3. Population densities before and after a collision with a boundary node. The effects of stationary (*a*) and moving (*b* and *c*) boundary nodes on the incoming populations are shown. The arrows indicate the velocity direction and the lengths of the solid lines are proportional to the population densities. The differences between population densities are highly exaggerated for clarity. Note that the effects of the moving boundary are the same in (*b*) and (*c*), because the velocity component parallel to the link direction is the same.

At each boundary node there are two incoming distributions $n_i(\boldsymbol{r}, t_+)$ and $n_{i'}(\boldsymbol{r}+\boldsymbol{c}_i, t_+)$, corresponding to velocities $\boldsymbol{c}_i$ and $\boldsymbol{c}_{i'}(\boldsymbol{c}_{i'} = -\boldsymbol{c}_i)$ parallel to the link connection $\boldsymbol{r}$ and $\boldsymbol{r}+\boldsymbol{c}_i$; the notation $n_i(\boldsymbol{r}, t_+) = n_i(\boldsymbol{r}, t)+\Delta_i(\boldsymbol{r}, t)$ is used to indicate the post-collision distribution (equation (2.15)). In some cases boundary nodes for two different link directions, perpendicular to one another, may be coincident (see figure 2); these are treated independently. The velocity of the boundary node $\boldsymbol{u}_b$ is determined by the solid particle velocity $\boldsymbol{U}$, angular velocity $\boldsymbol{\Omega}$, and centre of mass $\boldsymbol{R}$,

$$\boldsymbol{u}_b = \boldsymbol{U}+\boldsymbol{\Omega}\times(\boldsymbol{r}+\tfrac{1}{2}\boldsymbol{c}_i-\boldsymbol{R}). \tag{3.1}$$

By exchanging population density between n_i and $n_{i'}$ the local momentum density of the fluid can be modified to match the velocity of the solid particle surface at the boundary node, without affecting either the mass density or the stress, which depend only on the sum $n_i+n_{i'}$. Because the stress tensor is unaffected by the boundary-node interactions, it then follows that the hydrodynamic stick boundary condition applies right up to the solid surface, without any intervening boundary layer (Ladd & Frenkel 1990). This point will be discussed in more detail later. The mechanism for the boundary-node interactions is illustrated in figure 3. In figure 3(*a*) we see the two incoming populations, $n_i(\boldsymbol{r}, t_+)$ and $n_{i'}(\boldsymbol{r}+\boldsymbol{c}_i, t_+)$, interacting with a stationary boundary node. In this case, the populations are simply reflected back in the direction they came from (Frisch *et al.* 1987; Cornubert, d'Humières & Levermore 1991), so that

$$n_i(\boldsymbol{r}+\boldsymbol{c}_i, t+1) = n_{i'}(\boldsymbol{r}+\boldsymbol{c}_i, t_+) \quad \text{and} \quad n_{i'}(\boldsymbol{r}, t+1) = n_i(\boldsymbol{r}, t_+). \tag{3.2}$$

In figures 3(*b*) and 3(*c*) the effects of a moving object can be seen. In addition to reflection, population density is now transferred across the boundary node, in proportion to the velocity of the node $\boldsymbol{u}_b$,

$$\left.\begin{aligned} n_i(\boldsymbol{r}+\boldsymbol{c}_i, t+1) &= n_{i'}(\boldsymbol{r}+\boldsymbol{c}_i, t_+)+2a_1^{c_i}\rho\boldsymbol{u}_b\cdot\boldsymbol{c}_i, \\ n_{i'}(\boldsymbol{r}, t+1) &= n_i(\boldsymbol{r}, t_+)-2a_1^{c_i}\rho\boldsymbol{u}_b\cdot\boldsymbol{c}_i; \end{aligned}\right\} \tag{3.3}$$

these results are ensemble averages of our earlier boundary-node collision rules for lattice gases (Ladd & Frenkel 1989; Ladd 1991). Only the velocity component of the boundary node along the link direction ($\boldsymbol{c}_i$) is included in the calculation of population transfer; thus the outcome in figures 3(*b*) and 3(*c*) is the same. The general form for

the boundary-node interactions in (3.3) is determined by the requirement that the local mass density and stress tensor are conserved; thus rearrangements of population can only be made among pairs of opposite velocities. Furthermore, for stationary nodes the usual 'bounce-back' condition (3.2) must be recovered. The exact amount of population density transferred (i.e. the magnitude of the $\boldsymbol{u}_b \cdot \boldsymbol{c}_i$ term) is determined by the requirement that any distribution consistent with the boundary-node velocity $\boldsymbol{u}_b$ is stationary with respect to interactions with the boundary nodes. It is not obvious that (3.3) satisfies this condition, but it will be verified in the next paragraph that this is indeed so.

Let us now examine boundary-node interactions in more detail. From §2 we know that the distribution function at a node can be written as the sum of equilibrium, (2.5), and non-equilibrium contributions. The non-equilibrium part is proportional to $\overline{c_i c_i}$; the proportionality constant can be determined from (2.30), using the relation $\Sigma_i a_2^{c_i} \overline{c_{i\alpha} c_{i\beta} c_{i\gamma} c_{i\delta}} = \frac{1}{2}(\delta_{\alpha\gamma}\delta_{\beta\delta} + \delta_{\alpha\delta}\delta_{\beta\gamma} - \frac{2}{3}\delta_{\alpha\beta}\delta_{\gamma\delta})$:

$$n_i^{neq} = -a_2^{c_i}\, \boldsymbol{\sigma} : \overline{\boldsymbol{c}_i \boldsymbol{c}_i}. \tag{3.4}$$

Ignoring terms proportion to $\nabla \cdot \boldsymbol{u}$, the collisional stress tensor in (3.4) can be expressed in terms of velocity gradients (2.30),

$$\lambda n_i^{neq} = a_1^{c_i} \rho \boldsymbol{c}_i \boldsymbol{c}_i : \nabla \boldsymbol{u}; \tag{3.5}$$

here we have substituted $a_1^{c_i}$ for $\frac{2}{3}a_2^{c_i}$, (2.11). The post-collision distribution

$$n_i(\boldsymbol{r}, t_+) = n_i^{eq}(\boldsymbol{r}, t) + (1+\lambda)\, n_i^{neq}(\boldsymbol{r}, t)$$

(cf. (2.14) and (2.15) with $\lambda_B = -1$) is then given, to the same approximation, by

$$n_i(\boldsymbol{r}, t_+) = n_i(\boldsymbol{r}, t) + a_1^{c_i} \rho \boldsymbol{c}_i \boldsymbol{c}_i : \nabla \boldsymbol{u}(\boldsymbol{r}) = n_{i'}(\boldsymbol{r}, t) + 2a_1^{c_i} \rho \boldsymbol{u}(\boldsymbol{r}) \cdot \boldsymbol{c}_i + a_1^{c_i} \rho \boldsymbol{c}_i \boldsymbol{c}_i : \nabla \boldsymbol{u}(\boldsymbol{r}), \tag{3.6}$$

where the symmetries in the distribution functions for velocity directions i and i' have been exploited. If there is a boundary node located at $\boldsymbol{r} + \frac{1}{2}\boldsymbol{c}_i$, then the population $n_{i'}(\boldsymbol{r}, t+1)$ is modified according to (3.3), i.e.

$$n_{i'}(\boldsymbol{r}, t+1) = n_{i'}(\boldsymbol{r}, t) + 2a_1^{c_i} \rho [\boldsymbol{u}(\boldsymbol{r}) + \tfrac{1}{2}\boldsymbol{c}_i \cdot \nabla \boldsymbol{u}(\boldsymbol{r}) - \boldsymbol{u}_b(\boldsymbol{r} + \tfrac{1}{2}\boldsymbol{c}_i)] \cdot \boldsymbol{c}_i; \tag{3.7}$$

thus the distribution is stationary when the fluid velocity $\boldsymbol{u}(\boldsymbol{r} + \frac{1}{2}\boldsymbol{c}_i) = \boldsymbol{u}(\boldsymbol{r}) + \frac{1}{2}\boldsymbol{c}_i \cdot \nabla \boldsymbol{u}(\boldsymbol{r})$ is equal to the boundary-node velocity $\boldsymbol{u}_b$.

To illustrate the action of the boundary nodes more clearly, we consider, as an explicit example, planar Couette flow. Figure 4 shows a two-dimensional projection of the lattice-Boltzmann model onto the (x, y)-plane; the system is assumed to be time independent, and translationally invariant in the y- and z-directions. As an idealized model of a solid particle surface, two infinite planes of boundary nodes are set up, at $x = 0$ and $x = L$. In the fluid between the boundary surfaces ($0 < x < L$) there is a uniform velocity gradient $\nabla_x u_y(x) = \gamma$; outside the boundary planes, the fluid moves with uniform velocity equal to the wall velocity. Note that in this example, the lattice nodes are more conveniently set to half-integer values of x. The problem is to find the distribution function for this flow geometry that is stationary under the action of the boundary-node microrules, with velocities $\boldsymbol{u}_b(x = 0) = 0$ and $\boldsymbol{u}_b(x = L) = \gamma L$. A related problem, involving mixed stick–slip boundary conditions at a stationary wall, has been addressed by Cornubert *et al.* (1991).

The expected velocity distribution in a uniform velocity gradient can be constructed from the equilibrium distribution for Stokes flow (2.39) and the non-equilibrium distribution (3.5),

$$\lambda n_i^{neq} = a_1^{c_i} \rho c_{ix} c_{iy} \gamma. \tag{3.8}$$

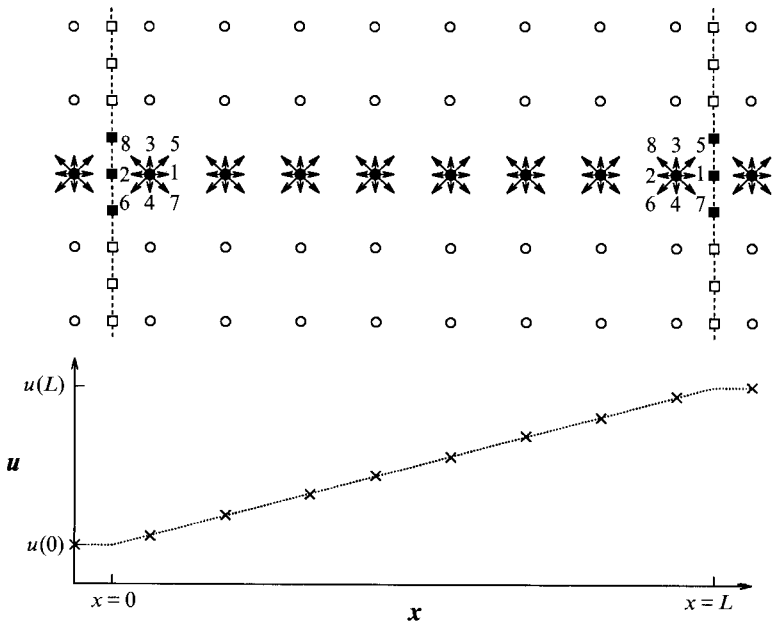

FIGURE 4. A two-dimensional projection of the lattice-Boltzmann fluid, bounded by plane walls. The boundary nodes are shown as squares and the boundary planes ($x = 0$ and $x = L$) by dashed lines. The circles are the lattice nodes; the set of nodes explicitly considered in the text are shown filled. The fluid between the walls is subjected to a velocity gradient by the relative motion of the walls; the fluid outside the walls moves with uniform velocity equal to the wall velocity. The labelling of velocity directions used in the text is also shown; velocity components in the z-direction have been projected onto the (x,y)-plane. There is an additional density of stationary particles (not shown), labelled 0, corresponding to velocities $[0, 0, \pm 1]$. The lower portion of the figure is a plot of the velocity profile, with the crosses showing the fluid velocity u_y at the nodes and the dotted line the interpolation between nodes.

Using the notation of figure 4, the velocity distribution function in the fluid ($0 < x < L$) can be written explicitly as

$$\left.\begin{aligned} &n_0(x) = 4, \\ &n_1(x) = 4, && n_2(x) = 4, \\ &n_3(x) = 4(1+2\gamma x), && n_4(x) = 4(1-2\gamma x), \\ &n_5(x) = (1+2\gamma x+2\gamma/\lambda), && n_6(x) = (1-2\gamma x+2\gamma/\lambda), \\ &n_7(x) = (1-2\gamma x-2\gamma/\lambda), && n_8(x) = (1+2\gamma x-2\gamma/\lambda); \end{aligned}\right\} \tag{3.9}$$

the densities n_0–n_4 have been multiplied by 4 to account for the number of projected velocities, and the mass density has, for convenience, been set equal to 24. The velocity distribution away from the boundaries is updated according to the usual time evolution of the lattice-Boltzmann equation. The post-collision distribution is computed from (1.10), (2.14), and (2.15), then propagated to the neighbouring nodes using (2.1). The new velocity distribution, denoted by n', is

$$\left.\begin{aligned} &n'_0(x) = 4, \\ &n'_1(x) = 4, && n'_2(x) = 4, \\ &n'_3(x) = 4(1+2\gamma x), && n'_4(x) = 4(1-2\gamma x), \\ &n'_5(x) = [1+2\gamma(x-1)+2\gamma(1+\lambda)/\lambda], && n'_6(x) = [1-2\gamma(x+1)+2\gamma(1+\lambda)/\lambda], \\ &n'_7(x) = [1-2\gamma(x-1)-2\gamma(1+\lambda)/\lambda], && n'_8(x) = [1+2\gamma(x+1)-2\gamma(1+\lambda)/\lambda], \end{aligned}\right\} \tag{3.10}$$

which is identical to the initial distribution (3.9), as required. For lattice-nodes adjacent to the solid–fluid boundaries, the update of some of the population densities is affected by the boundary nodes (3.3): explicitly

$$\left.\begin{aligned} n'_5(\tfrac{1}{2}) &= [1-2\gamma(\tfrac{1}{2})+2\gamma(1+\lambda)/\lambda], \\ n'_7(\tfrac{1}{2}) &= [1+2\gamma(\tfrac{1}{2})-2\gamma(1+\lambda)/\lambda], \\ n'_6(L-\tfrac{1}{2}) &= [1+2\gamma(L-\tfrac{1}{2})+2\gamma(1+\lambda)/\lambda]-4\gamma L, \\ n'_8(L-\tfrac{1}{2}) &= [1-2\gamma(L-\tfrac{1}{2})-2\gamma(1+\lambda)/\lambda]+4\gamma L, \end{aligned}\right\} \tag{3.11}$$

which, once again, is identical to the initial distribution (3.9). Thus the boundary-node collision rules generate an exact linear shear flow; this is because they maintain the second-order accuracy of the pure fluid model. Furthermore, the velocity distributions outside and inside the particle are isolated from one another; thus a sharp change in velocity gradient from the inside to the outside the particle surface can be supported, as illustrated in figure 4.

As a result of the boundary-node interactions (3.3), forces are exerted on the solid particles at the boundary nodes, i.e.

$$\begin{aligned} \boldsymbol{f}(\boldsymbol{r}+\tfrac{1}{2}\boldsymbol{c}_i, t+\tfrac{1}{2}) &= -[n_i(\boldsymbol{r}+\boldsymbol{c}_i, t+1)-n_{i'}(\boldsymbol{r}, t+1)-n_i(\boldsymbol{r}, t_+)+n_{i'}(\boldsymbol{r}+\boldsymbol{c}_i, t_+)]\,\boldsymbol{c}_i \\ &= 2[n_i(\boldsymbol{r}, t_+)-n_{i'}(\boldsymbol{r}+\boldsymbol{c}_i, t_+)-2a_1^{c_i}\rho\boldsymbol{u}_b\cdot\boldsymbol{c}_i]\,\boldsymbol{c}_i; \end{aligned} \tag{3.12}$$

thus momentum is exchanged locally between the fluid and the solid particle, but the combined momentum of solid and fluid is conserved. The forces and torques on the solid particle are obtained by summing $\boldsymbol{f}(\boldsymbol{r}+\frac{1}{2}\boldsymbol{c}_i)$ and $(\boldsymbol{r}+\frac{1}{2}\boldsymbol{c}_i)\times\boldsymbol{f}(\boldsymbol{r}+\frac{1}{2}\boldsymbol{c}_i)$ over all the boundary nodes associated with a particular particle. As an example, (3.12) can be used to compute the drag force per unit area on a planar wall adjacent to a steadily shearing fluid. We compute the force on one face of each solid boundary surface, assuming that the fluid on the other side is moving uniformly with the velocity of the boundary (as shown in figure 4) and therefore exerts no force on the wall; this corresponds to replacing one of the distributions in (3.12) by its equilibrium form (2.39) with a velocity equal to the wall velocity. Using the distributions at t_+ just after the molecular collision process ((3.9) with $1/\lambda$ replaced by $(1+\lambda)/\lambda$) the wall forces are found to be

$$\left.\begin{aligned} f_y(0) &= 2[-n_6(\tfrac{1}{2}, t_+)+n_8(\tfrac{1}{2}, t_+)] = -4(2/\lambda+1)\,\gamma = \eta\gamma, \\ f_y(L) &= 2[n_5(L-\tfrac{1}{2}, t_+)-n_7(L-\tfrac{1}{2}, t_+)-4\gamma L] = 4(2/\lambda+1)\,\gamma = -\eta\gamma; \end{aligned}\right\} \tag{3.13}$$

the last equality follows from summing the collisional and lattice contributions to the viscosity (2.34), using $\rho = 24$. Thus the wall force is computed exactly for linear shear flows.

As a preliminary application of the method to time-dependent flows, we consider the evolution of the flow field from an impulsively started flat plate. The geometry is similar to figure 4, with the plates being sufficiently far apart that they do not interact over the duration of the simulation. We focus on a single plate ($x = 0$). Initially the system is at rest; at $t = 0$, an impulsive force gives the plate a constant velocity $[0, U, 0]$. In this problem it is again convenient to define the lattice nodes at half-integer values of x, and for the fluid to reside at the lattice nodes at half-integer values of the time; then the boundary conditions at the plate are applied at $x = 0$ and $t = 0$ precisely. We compute numerically the evolution of the flow field $[0, u(x, t), 0]$, created by the diffusion of vorticity into the fluid, and compare with the analytic solutions for the velocity field (Batchelor 1967)

$$u(x, t) = U\{1-\Phi[x/(4\nu t)^{\frac{1}{2}}]\}, \tag{3.14}$$

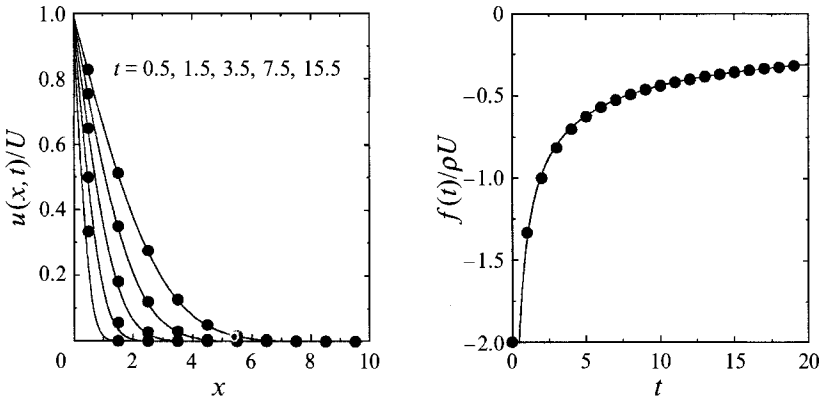

FIGURE 5. Flow induced by an impulsively loaded flat plate, $U(t) = 0$ for $t < 0$ and $U(t) = U$ for $t \geqslant 0$. The plots show the velocity field and force per unit area on the wall at various times; the solid circles are the numerical simulations and the solid lines are analytical results (Batchelor 1967).

and the force per unit area

$$f(t) = \eta \nabla_x u(0,t) = -\eta U(\pi \nu t)^{-\frac{1}{2}}; \tag{3.15}$$

$\nu = \eta/\rho$ is the kinematic viscosity of the fluid and Φ is the error function. The results are shown in figure 5 (for a viscosity $\nu = \frac{1}{6}$) at several different times. It can be seen that there is complete agreement, except at very short times and distances. This simple test implies that both stationary and time-dependent flows can be simulated accurately, as will be confirmed by further results in Part 2.

Next, consider flow perpendicular to the wall. The incompressibility condition means that there can be no velocity gradients in steady flow; thus the fluid velocity and the wall velocities are $[u, 0, 0]$. For this flow the model shown in figure 4 can be further simplified to just three velocity directions: stationary particles, and particles moving in the positive and negative x-directions. The projected distributions are

$$n_0(x) = 12, \quad n_1(x) = 6(1+2u), \quad n_2(x) = 6(1-2u). \tag{3.16}$$

Clearly this distribution is stationary with the respect to the evolution of the lattice-Boltzmann equation; it is also stationary with respect to the boundary-node update rules (3.3). However, this is not the only stationary distribution that satisfies the boundary conditions. A more general form for the distribution function, which exhibits a two-time-step repeat cycle is

$$n_0(x) = 12, \quad n_1(x) = 6(1+2u+(-1)^{t+x}2w), \quad n_2(x) = 6(1-2u-(-1)^{t+x}2w); \tag{3.17}$$

it is straightforward to verify that this distribution also satisfies both the time evolution equation and the boundary conditions at the walls. Thus the fluid has a uniform momentum ρu and a 'staggered' momentum $(-1)^{t+x}\rho w$. Staggered momenta are an artifact of all lattice models (Zanetti 1989); the precise value of the staggered momentum depends on the channel width (in this example) and the initial conditions. Although staggered momenta cannot arise spontaneously in the fluid, they can be generated at solid surfaces, as seen in this example. However, it can be shown by techniques similar to those used above that staggered momentum parallel to the walls is damped by the boundary conditions, so that for plane Couette flow the steady solutions have no staggered momentum component.

In the more complex geometries that are of interest in particulate suspensions, it is

impossible to analyse the staggered momenta analytically. Numerical results show that large oscillations in particle torques can be built up by a feedback mechanism in which the staggered momenta are fed by ever-increasing angular velocities of the particles. To overcome these instabilities we average the force and fluid velocity over two successive time steps which effectively cancels out the staggered momentum contribution. In the above example, this gives a uniform flow field with velocity $[u, 0, 0]$ regardless of the magnitude of the staggered momenta. Since the forces at the boundary nodes are generated at the half-integer time steps, the smoothly varying force $\bar{\boldsymbol{f}}$ at the intermediate integer time is

$$\bar{\boldsymbol{f}}(\boldsymbol{r}+\tfrac{1}{2}\boldsymbol{c}_i, t) = \tfrac{1}{2}[\boldsymbol{f}(\boldsymbol{r}+\tfrac{1}{2}\boldsymbol{c}_i, t-\tfrac{1}{2})+\boldsymbol{f}(\boldsymbol{r}+\tfrac{1}{2}\boldsymbol{c}_i, t+\tfrac{1}{2})]. \tag{3.18}$$

We can calculate the smooth part of the fluid velocity field at half-integer time steps in a similar way,

$$\bar{\boldsymbol{u}}(\boldsymbol{r}, t+\tfrac{1}{2}) = \tfrac{1}{2}[\boldsymbol{u}(\boldsymbol{r}, t)+\boldsymbol{u}(\boldsymbol{r}, t+1)], \tag{3.19}$$

or at integer time steps using the three-point formula

$$\bar{\boldsymbol{u}}(\boldsymbol{r}, t) = \tfrac{1}{4}[\boldsymbol{u}(\boldsymbol{r}, t-1)+2\boldsymbol{u}(\boldsymbol{r}, t)+\boldsymbol{u}(\boldsymbol{r}, t+1)]. \tag{3.20}$$

The velocities of finite-mass particles (as opposed to infinitely massive fixed objects) are updated every two time steps,

$$\boldsymbol{U}(t+1) = \boldsymbol{U}(t-1)+2M^{-1}\boldsymbol{F}(t), \quad \boldsymbol{\Omega}(t+1) = \boldsymbol{\Omega}(t-1)+2\boldsymbol{I}^{-1}\cdot\boldsymbol{T}(t). \tag{3.21}$$

The particle mass M and moment of inertia $\boldsymbol{I}$ are preassigned parameters which control the rate at which particles respond to the fluid flow; usually M and $\boldsymbol{I}$ are on the order of several thousands (in lattice units). Since the particle velocities vary slowly on the timescale of a lattice-Boltzmann cycle, the precise form for the update is usually not too important; however, it is important to use time-smoothed forces and torques, as described in (3.18).

So far only flows with linear velocity profiles have been considered. In the next and last example a stationary, two-dimensional channel flow is examined. The geometry is again shown in figure 4, this time with stationary walls ($\boldsymbol{u}_b = 0$). The fluid is driven by a pressure gradient, which is represented in the simulation by a uniform force density in the fluid. Thus a constant increment Δj_y is applied to the y-momentum at each node, so that the pressure gradient down the channel is $\nabla_y p = \Delta j_y$. The fluid velocity at each node is measured after half the force has been applied; it was found empirically that this prescription gives the fastest convergence as a function of system size. The steady flow profiles are compared with the analytic solution,

$$u_y(x) = (\Delta j_y/2\eta)\, x(L-x), \tag{3.22}$$

in figure 6. It can be seen that the agreement is very good for channels more than about 9 lattice spacings wide. Furthermore, the force on the walls is exact, no matter what the channel width. This result follows from the balance between forces on the walls and the total force from the pressure gradient. Since the pressure forces are distributed equally on the walls it follows that the wall force per unit area $f = \frac{1}{2}\Delta j_y L$, which is the correct result for Poiseuille flow.

In this section it has been shown that moving solid boundaries can be incorporated into a lattice-Boltzmann simulation, and it has been indicated how they function for a few simple examples. In Part 2 numerical results for spherical particles are described, both in periodic arrays and random assemblies. Results are compared with known analytic and numerical solutions of the creeping-flow and Navier–Stokes equations.

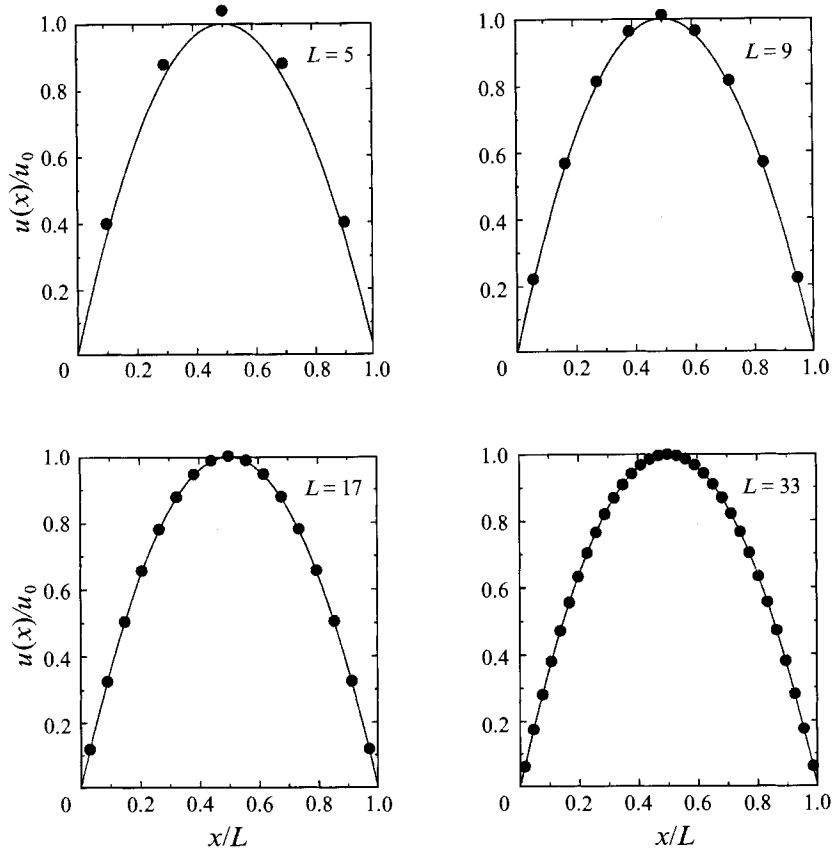

FIGURE 6. Poiseuille flow in two-dimensional channels for different channel widths, L. The simulated velocities (solid circles) are scaled by the theoretical maximum value $u_0 = \Delta j_y L^2/8\eta$.

4. Fluctuations

In recent years, it has become increasingly apparent that the lattice-Boltzmann equation is a much better simulation tool for hydrodynamics than lattice gases. However, in its normal state the lattice-Boltzmann equation cannot model the molecular fluctuations in the solvent that give rise to Brownian motion. Of course in many situations Brownian motion is unimportant, but, for suspensions of sub-micron-sized particles, it is a fundamental component of the dynamics. It has been shown recently (Ladd 1993) that fluctuations can be incorporated into the lattice-Boltzmann equation, within the framework of fluctuating hydrodynamics (Landau & Lifshitz 1959), by adding a random component to the fluid stress tensor. Numerical tests showed that the resulting particle motion, in dilute to concentrated suspensions, closely matched experimental results (Zhu *et al.* 1992; Kao, Yodh & Pine 1993), even at very short times where particle inertia plays an important role. In this section a basic theory of fluctuations, as it applies to the lattice-Boltzmann model, is described; in Part 2 numerical tests of the method for particulate suspensions of spheres will be reported.

The fundamental idea behind fluctuating hydrodynamics is that, on lengthscales and timescales intermediate between the molecular and the hydrodynamic, thermally induced fluctuations can be reduced to random fluctuations in the fluxes of the conserved variables, i.e. the stress tensor and perhaps the heat flux also. At longer wavelengths, fluctuations are unimportant and the usual equations of hydrodynamics

are recovered; at short scales the hydrodynamic picture breaks down and only a fully molecular description will suffice. Since the fluxes are included explicitly in a lattice-Boltzmann simulation, it is plausible that molecular fluctuations can be modelled realistically on intermediate scales, even though the details of the microscopic interactions are different. In the present context, this means that the time evolution of the velocity distribution includes a stochastic term $n_i'(\boldsymbol{r}, t)$, representing the thermally induced fluctuations in the stress tensor:

$$n_i(\boldsymbol{r}+\boldsymbol{c}_t, t) = n_i(\boldsymbol{r}, t)+\Delta_i(\boldsymbol{r}, t)+n_i'(\boldsymbol{r}, t), \tag{4.1}$$

where n' is chosen so that only its stress moment is non-zero (cf. (3.4)),

$$n_i' = -a_2^{c_i}\,\sigma_{\alpha\beta}'\,\overline{c_{i\alpha}c_{i\beta}}. \tag{4.2}$$

These random stress fluctuations $\sigma_{\alpha\beta}'$ are uncorrelated in space and time (Landau & Lifshitz 1959) and are sampled from a Gaussian distribution,

$$\langle\sigma_{\alpha\beta}'(\boldsymbol{r}, t)\,\sigma_{\gamma\delta}'(\boldsymbol{r}', t')\rangle = A\delta_{rr'}\,\delta_{tt'}(\delta_{\alpha\gamma}\,\delta_{\beta\delta}+\delta_{\alpha\delta}\,\delta_{\beta\gamma}-\tfrac{2}{3}\delta_{\alpha\beta}\,\delta_{\gamma\delta}); \tag{4.3}$$

the choice of the variance A serves to define the effective temperature of the fluid. We can determine the relationship between A and the temperature via the fluctuation-dissipation theorem.

It is convenient in what follows to work in Fourier space, defining the Fourier transform of the velocity distribution function as

$$n_i(\boldsymbol{k}, t) = \sum_{\boldsymbol{r}\in V} \mathrm{e}^{-\mathrm{i}\boldsymbol{k}\cdot\boldsymbol{r}} n_i(\boldsymbol{r}, t), \tag{4.4}$$

where the sum is over all the lattice points in the periodic unit cell. Then the equation for momentum conservation (2.17) can be written as

$$\sum_i [\mathrm{e}^{\mathrm{i}\boldsymbol{k}\cdot\boldsymbol{c}_i} n_i(\boldsymbol{k}, t+1)-n_i(\boldsymbol{k}, t)]\,\boldsymbol{c}_i = 0; \tag{4.5}$$

we will attempt to cast this equation into the form of a Langevin equation for the transverse (or solenoidal) momentum fluctuations $\boldsymbol{j}_\perp(\boldsymbol{k}, t) = (\boldsymbol{I}-\hat{\boldsymbol{k}}\hat{\boldsymbol{k}})\cdot\boldsymbol{j}(\boldsymbol{k}, t)$ ($\hat{\boldsymbol{k}}$ is the unit vector $\boldsymbol{k}/k$). Expanding the exponential, we have

$$\boldsymbol{j}_\perp(\boldsymbol{k}, t+1)-\boldsymbol{j}_\perp(\boldsymbol{k}, t)+\mathrm{i}\boldsymbol{k}\cdot\overline{\boldsymbol{\Pi}}(\boldsymbol{k}, t+1)\cdot(\boldsymbol{I}-\hat{\boldsymbol{k}}\hat{\boldsymbol{k}})-\tfrac{1}{6}k^2\boldsymbol{j}_\perp(\boldsymbol{k}, t+1) = O(k^4), \tag{4.6}$$

where $\overline{\boldsymbol{\Pi}}(\boldsymbol{k}, t) = \Sigma_i n_i(\boldsymbol{k}, t)\,\overline{\boldsymbol{c}_i\boldsymbol{c}_i}$ is the traceless part of the momentum flux. (The third-order terms in k involve fourth-order moments of n_i, which are proportional to the identity tensor. Thus the k^3 contributions lie parallel to $\boldsymbol{k}$ and have no transverse component.) To obtain a Langevin equation, the momentum flux is divided into a slowly relaxing dissipative part and a rapidly varying fluctuating part. In §2, it was shown that on the shorter ϵ^{-1} timescale, the stress relaxed to its Navier–Stokes form (2.30), whereas the velocity gradients varied on a longer ϵ^{-2} timescale. Thus the fluctuating stress $\boldsymbol{\Sigma}$ is defined as

$$\Sigma_{\alpha\beta} = -[\overline{\Pi}_{\alpha\beta}-(1/3\lambda)\,(\nabla_\alpha j_\beta+\nabla_\beta j_\alpha-\tfrac{2}{3}\nabla_\gamma j_\gamma\,\delta_{\alpha\beta})], \tag{4.7}$$

ignoring density fluctuations (because they do not couple to the transverse momentum flux) and nonlinear $\rho\boldsymbol{uu}$ terms (because we are examining small lengthscales where the Reynolds number is negligible). Combining (4.6) and (4.7), and summing the collisional $(1/3\lambda)$ and lattice $(\frac{1}{6})$ contributions to the viscosity (2.34), we obtain a discrete Langevin equation for the transverse momentum fluctuations,

$$\boldsymbol{j}_\perp(\boldsymbol{k}, t+1)-\boldsymbol{j}_\perp(\boldsymbol{k}, t)+\nu k^2\boldsymbol{j}_\perp(\boldsymbol{k}, t+1) = \mathrm{i}\boldsymbol{k}\cdot\boldsymbol{\Sigma}(\boldsymbol{k}, t+1)\cdot(\boldsymbol{I}-\hat{\boldsymbol{k}}\hat{\boldsymbol{k}}), \tag{4.8}$$

with a random force $i\boldsymbol{k}\cdot\boldsymbol{\Sigma}(\boldsymbol{k},t+1)\cdot(\boldsymbol{1}-\hat{\boldsymbol{k}}\hat{\boldsymbol{k}})$. The solution of this equation is described in the Appendix; the result is (cf. (A 8))

$$2\nu\langle \boldsymbol{j}_\perp(\boldsymbol{k})\cdot\boldsymbol{j}_\perp(-\boldsymbol{k})\rangle = \sum_{t=-\infty}^{\infty}\langle \hat{\boldsymbol{k}}\cdot\boldsymbol{\Sigma}(\boldsymbol{k},t)\cdot(\boldsymbol{1}-\hat{\boldsymbol{k}}\hat{\boldsymbol{k}})\cdot\boldsymbol{\Sigma}(-\boldsymbol{k},0)\cdot\hat{\boldsymbol{k}}\rangle. \tag{4.9}$$

The effective temperature of the fluid can be determined by equating the fluctuations in momentum to those in real fluids; for a molecular fluid of N particles of mass m,

$$\langle \boldsymbol{j}_\perp(\boldsymbol{k})\cdot\boldsymbol{j}_\perp(-\boldsymbol{k})\rangle = \frac{2}{3}\left\langle \sum_{i,j=1}^{N} \mathrm{e}^{-i\boldsymbol{k}\cdot\boldsymbol{R}_{ij}}\boldsymbol{v}_i\cdot\boldsymbol{v}_j\right\rangle = 2Nmk_BT = 2\rho Vk_BT, \tag{4.10}$$

where the factor $\frac{2}{3}$ comes from the missing longitudinal fluctuations. In the long-wavelength limit we can isotropically average over the directions of $\boldsymbol{k}$, with the result

$$\lim_{k\to 0}\langle \hat{\boldsymbol{k}}\cdot\boldsymbol{\Sigma}(\boldsymbol{k},t)\cdot(1-\hat{\boldsymbol{k}}\hat{\boldsymbol{k}})\cdot\boldsymbol{\Sigma}(-\boldsymbol{k},0)\cdot\hat{\boldsymbol{k}}\rangle = \tfrac{1}{5}\langle \boldsymbol{\Sigma}(t):\boldsymbol{\Sigma}(0)\rangle = 2\langle \Sigma_{xy}(t)\Sigma_{xy}(0)\rangle, \tag{4.11}$$

where

$$\boldsymbol{\Sigma}(t) = \lim_{k\to 0}\boldsymbol{\Sigma}(\boldsymbol{k},t) = \sum_{r\in V}\boldsymbol{\sigma}(\boldsymbol{r},t). \tag{4.12}$$

Combining (4.9)–(4.11) leads to a fluctuation formula for the viscosity,

$$\eta Vk_BT = \tfrac{1}{2}\langle \Sigma_{xy}(0)\Sigma_{xy}(0)\rangle + \sum_{t=1}^{\infty}\langle \Sigma_{xy}(t)\Sigma_{xy}(0)\rangle, \tag{4.13}$$

which is an analogue of the Green–Kubo relation for molecular liquids (Hansen & McDonald 1986). The summation in (4.13) is the equivalent of a Simpson's rule approximation to the time integral that appears in the usual Green–Kubo formulae. In Part 2 this expression is used to calculate suspension viscosities, replacing the fluid stress tensor with the combined stress tensor of the solid and fluid phases.

Let us now consider the time evolution of the stress tensor in the pure fluid. The total stress fluctuations $\boldsymbol{\Sigma}$ in a volume V are independent of the propagation of population density; they vary only because of collisions and random fluctuations. Thus the time evolution of $\boldsymbol{\Sigma}$ including the random fluctuations can be written as

$$\boldsymbol{\Sigma}(t+1) = (1+\lambda)\boldsymbol{\Sigma}(t) + \sum_{r\in V}\boldsymbol{\sigma}'(\boldsymbol{r},t). \tag{4.14}$$

Since $\langle \boldsymbol{\sigma}'(\boldsymbol{r},t)\boldsymbol{\Sigma}(0)\rangle = 0$ for all $t \geqslant 0$, the time correlation function of the stress fluctuations can be written in terms of equal-time correlations (cf. (A 4)),

$$\langle \boldsymbol{\Sigma}(t)\boldsymbol{\Sigma}(0)\rangle = (1+\lambda)^t\langle \boldsymbol{\Sigma}(0)\boldsymbol{\Sigma}(0)\rangle; \tag{4.15}$$

thus from (4.13) and (2.34) the effective temperature can be related to the equal-time stress fluctuations,

$$\rho Vk_BT = 3\langle \Sigma_{xy}^2\rangle. \tag{4.16}$$

Finally, we must relate the equal-time stress fluctuations to the fluctuations in the random stress tensor. This can be done by noting that (4.14) is a discretized Langevin equation for the stress tensor, for which the random forces at different times are uncorrelated (see the Appendix). Since $|(1+\lambda)| < 1$, the equal-time correlation function is given by ((A 7) and (4.3))

$$\langle \Sigma_{\alpha\beta}\Sigma_{\gamma\delta}\rangle = \frac{AV}{1-(1+\lambda)^2}(\delta_{\alpha\gamma}\delta_{\beta\delta}+\delta_{\alpha\delta}\delta_{\beta\gamma}-\tfrac{2}{3}\delta_{\alpha\beta}\delta_{\gamma\delta}). \tag{4.17}$$

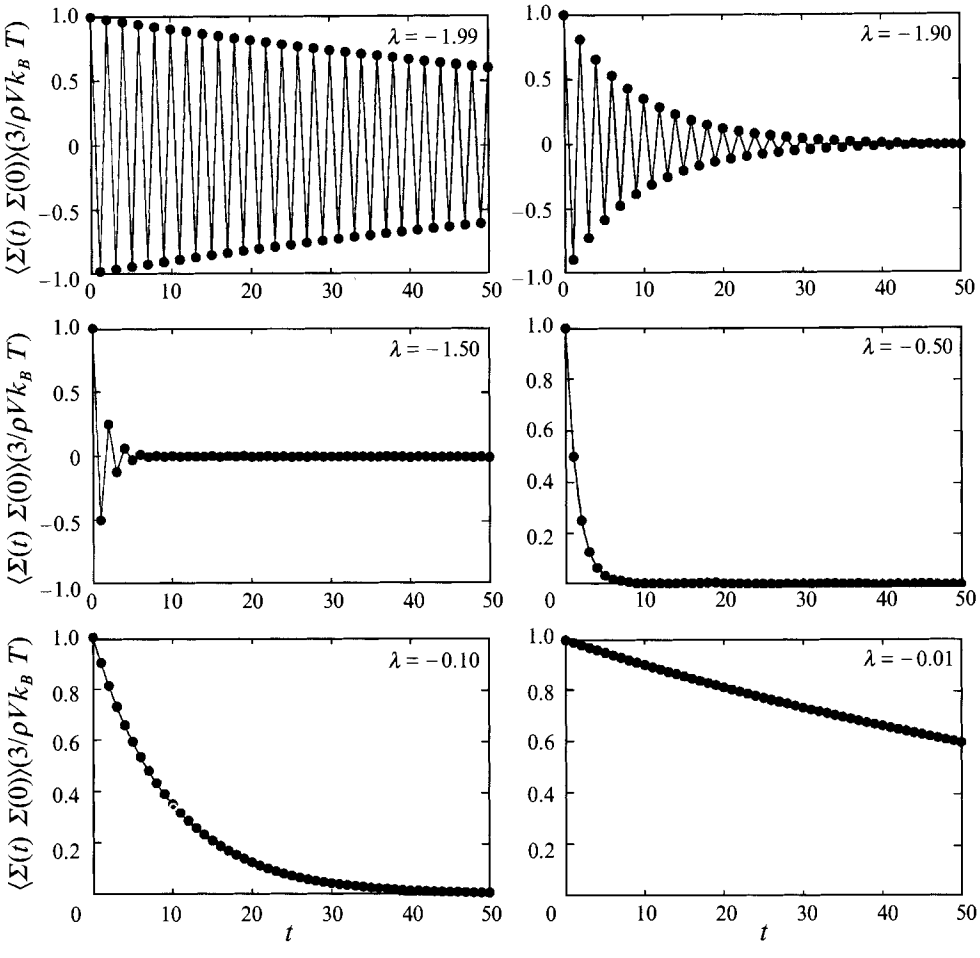

FIGURE 7. Stress–stress correlation function for a lattice-Boltzmann fluid. Numerical results (solid circles) and theoretical results from (4.15) (solid lines) are shown for different values of λ.

Then, from (4.16) and (4.17)

$$A = (\tfrac{1}{3}\rho k_B T)[1-(1+\lambda)^2] = 2\eta k_B T\lambda^2, \tag{4.18}$$

which is the fluctuation-dissipation relation for our fluctuating lattice-Boltzmann equation. It defines the effective temperature of the fluid so that the dissipation, (2.34), and fluctuation, (4.13), expression for the viscosity are consistent.

Some numerical tests of the fluctuating lattice-Boltzmann equation are illustrated in figure 7. Here simulation results for the stress–stress correlation function are compared with theoretical results, (4.15), for a range of values of λ, covering kinematic viscosities from about 10^{-3} to about 30. For both the over-relaxing collision operators ($-2 < \lambda < -1$), where the stress tensor changes sign at every time step, and for the under-relaxing collision operators ($-1 < \lambda < 0$) the agreement between theory and simulation is perfect. In general, values of λ close to -1 are chosen, to minimize the relaxation time of the stress fluctuations. The special case $\lambda = -1$ is particularly useful; here the stress fluctuations decay instantaneously, since only the random part of the stress tensor gets propagated at each time step (see (4.14)). In this limit the expression for A, (4.18), reduces to the Landau–Lifshitz (1959) result $A = 2\eta k_B T$.

5. Conclusions

In this paper the theoretical foundation for a new simulation technique for particulate suspensions has been described. Much of the theory underlying this work is now well understood; in particular the macroscopic fluid dynamics arising from the various lattice-Boltzmann models, and the modelling of hydrodynamic stick boundary conditions by local modifications to particle populations. The computational effectiveness of the method will be demonstrated in Part 2. The inclusion of fluctuations in the stress tensor is a more recent development (Ladd 1993) and is less well understood. Nevertheless, we have been able to derive discrete analogues of the basic equations of fluctuating hydrodynamics; again the numerical tests reported in Part 2 provide convincing evidence of the correctness of the approach.

This work was supported by the U.S. Department of Energy and Lawrence Livermore National Laboratory under Contract No. W-7405-Eng-48.

Appendix. Discrete Langevin equation

The discrete Langevin equation, (4.8) or (4.14), is of the general form

$$j(t+1)-j(t) = -\alpha j(t)+f(t), \tag{A 1}$$

where α is a positive constant controlling the rate of dissipation ($0 < \alpha < 2$), and $f(t)$ is the random force. The random force has the usual property

$$\langle f(t)j(t')\rangle = 0, \tag{A 2}$$

for all $t \geqslant t'$. We can rewrite (A 1) as

$$j(t+t') = (1-\alpha)^{t'}j(t)+\sum_{s=1}^{t'}(1-\alpha)^{s-1}f(t+t'-s), \tag{A 3}$$

and from (A 2) the time correlation function can be expressed in terms of equal-time fluctuations,

$$\langle j(t+t')j(t)\rangle = (1-\alpha)^{t'}\langle j(t)j(t)\rangle. \tag{A 4}$$

The equal-time correlations, measured from some initial time ($t = 0$), are given by

$$\langle j(t')j(t')\rangle = (1-\alpha)^{2t'}\langle j(0)j(0)\rangle+\sum_{s=1}^{t'}\sum_{s'=1}^{t'}(1-\alpha)^{s+s'-2}\langle f(t'-s)f(t'-s')\rangle. \tag{A 5}$$

In the long-time ($t' \to \infty$) limit the system loses all memory of its initial conditions; (A 5) can then be simplified by a change of variables, $s_{\pm} = s \pm s'$:

$$\begin{aligned}\langle j^2\rangle &= \sum_{s_-=-\infty}^{\infty}(1-\alpha)^{|s_-|}\langle f(s_-)f(0)\rangle\sum_{s_+=0}^{\infty}(1-\alpha)^{2s_+}\\ &= \frac{1}{2\alpha-\alpha^2}\sum_{s_-=-\infty}^{\infty}(1-\alpha)^{|s_-|}\langle f(s_-)f(0)\rangle.\end{aligned} \tag{A 6}$$

In the special case that the random force is delta-function correlated in time (as in (4.14)), then

$$\langle j^2\rangle = \frac{\langle f^2\rangle}{2\alpha-\alpha^2}. \tag{A 7}$$

In the more general case (i.e. in (4.8)) the random force has a finite but short relaxation time τ_R. Here a simple result can only be obtained for sufficiently small values of α that $(1-\alpha)^{\tau_R} \approx 1$:

$$\langle j^2 \rangle = \frac{1}{2\alpha} \sum_{t=-\infty}^{\infty} \langle f(t) f(0) \rangle; \tag{A 8}$$

this result applies to (4.8) in the limit $\boldsymbol{k} \to 0$.

REFERENCES

ALLEN, M. P. & TILDESLEY, D. J. 1987 *Computer Simulation of Liquids*. Clarendon.

BATCHELOR, G. K. 1967 *An Introduction to Fluid Dynamics*. Cambridge University Press.

BIRD, G. A. 1976 *Molecular Gas Dynamics*. Oxford University Press.

BIRD, G. A. 1990 The direct simulation Monte Carlo method: Current status and perspectives. In *Microscopic Simulations of Complex Flows* (ed. M. Marechal). Plenum.

BOSSIS, G. & BRADY, J. F. 1987 Self-diffusion of Brownian particles in concentrated suspensions under shear. *J. Chem. Phys.* **87**, 5437.

BRADY, J. F. & BOSSIS, G. 1988 Stokesian dynamics. *Ann. Rev. Fluid. Mech.* **20**, 111.

CHAPMAN, S. & COWLING, T. G. 1960 *The Mathematical Theory of Non-Uniform Gases*. Cambridge University Press.

CHEN, S., WANG, Z., SHAN, X. & DOOLEN, G. D. 1992 Lattice Boltzmann computational fluid dynamics in three dimension. *J. Statist Phys* **68**, 379.

CORNUBERT, R., D'HUMIÈRES, D. & LEVERMORE, C. D. 1991 A Knudsen layer theory for lattice gases. *Physica* D **47**, 241.

DURLOFSKY, L., BRADY, J. F. & BOSSIS, G. 1987 Dynamic simulation of hydrodynamically interacting particles. *J. Fluid Mech.* **180**, 21.

ERMAK, D. L. & MCCAMMON, J. A. 1978 Brownian dynamics with hydrodynamic interactions. *J. Chem. Phys.* **69**, 1352.

FOGELSON, A. L. & PESKIN, C. S. 1988 A fast numerical method for solving the three-dimensional Stokes equations in the presence of suspended particles. *J. Comput. Phys.* **79**, 50.

FRISCH, U., HASSLACHER, B. & POMEAU, Y. 1986 Lattice gas automata for the Navier–Stokes equation. *Phys. Rev. Lett.* **56**, 1505.

FRISCH, U., D'HUMIÈRES, D., HASSLACHER, B., LALLEMAND, P., POMEAU, Y. & RIVET, J.-P. 1987 Lattice gas hydrodynamics in two and three dimension. *Complex Systems* **1**, 649.

HANSEN, J. P. & MCDONALD, I. R. 1986 *Theory of Simple Liquids*. Academic.

HAPPEL, J. & BRENNER, H. 1986 *Low-Reynolds Number Hydrodynamics*. Martinus Nijhoff.

HIGUERA, F., SUCCI, S. & BENZI, R. 1989 Lattice gas dynamics with enhanced collisions. *Europhys. Lett.* **9**, 345.

HOEF, M. A. VAN DER 1992 Simulation study of diffusion in lattice-gas fluids and colloids. PhD thesis, University of Utrecht, Utrecht, Netherlands.

HOEF, M. A. VAN DER, FRENKEL, D. & LADD, A. J. C. 1991 Self-diffusion of colloidal particles in a two-dimensional suspension: are deviations from Fick's law experimentally observable? *Phys. Rev. Lett.* **67**, 3459.

HOOGERBRUGGE, P. J. & KOELMAN, J. M. V. A. 1992 Simulating microscopic hydrodynamic phenomena with dissipative particle dynamics. *Europhys. Lett.* **19**, 155.

KAO, M. H., YODH, A. G. & PINE, D. J. 1993 Observation of Brownian motion on the time scale of the hydrodynamic interaction. *Phys. Rev. Lett.* **70**, 242.

KARRILA, S. J., FUENTES, Y. O. & KIM, S. 1989 Parallel computational strategies for hydrodynamic interactions between rigid particles of arbitrary shape in a viscous fluid. *J. Rheol.* **33**, 913.

KOELMAN, J. M. V. A. & HOOGERBRUGGE, P. J. 1993 Dynamic simulations of hard-sphere suspensions under steady shear. *Europhys. Lett.* **21**, 363.

LADD, A. J. C. 1988 Hydrodynamic interactions in a suspension of spherical particles. *J. Chem. Phys.* **88**, 5051.

LADD, A. J. C. 1991 Dissipative and fluctuating hydrodynamic interactions between suspended solid particles via lattice-gas cellular automata. In *Computer Simulation in Materials Science* (ed. M. Meyer & V. Pontikis). Kluwer.

LADD, A. J. C. 1993 Short-time motion of colloidal particles: Numerical simulation via a fluctuating lattice-Boltzmann equation. *Phys. Rev. Lett.* **70**, 1339.

LADD, A. J. C. 1994 Numerical simulations of particulate suspensions via a discretized Boltzmann equation. Part 2. Numerical results. *J. Fluid Mech.* **271**, 311.

LADD, A. J. C., COLVIN, M. E. & FRENKEL, D. 1988 Application of lattice-gas cellular automata to the Brownian motion of solids in suspension. *Phys. Rev. Lett.* **60**, 975.

LADD, A. J. C. & FRENKEL, D. 1989 Dynamics of colloidal dispersions via lattice-gas models of an incompressible fluid. In *Cellular Automata and Modeling of Complex Physical Systems* (ed. P. Manneville, N. Boccara, G. Y. Vichniac & R. Bidaux. Springer.

LADD, A. J. C. & FRENKEL, D. 1990 Dissipative hydrodynamic interactions via lattice-gas cellular automata. *Phys. Fluids* A **2**, 1921.

LANDAU, L. D. & LIFSHITZ, E. M. 1959 *Fluid Mechanics*. Addison-Wesley.

MCNAMARA, G. R. & ALDER, B. J. 1992 Lattice Boltzmann simulation of high Reynolds number fluid flow in two dimensions. In *Microscopic Simulations of Complex Hydrodynamic Phenomena* (ed. M. Mareschal & B. L. Holian). Plenum.

MCNAMARA, G. R. & ALDER, B. J. 1993 Analysis of the lattice Boltzmann treatment of hydrodynamics. *Physica* A **194**, 218.

MCNAMARA, G. R. & ZANETTI, G. 1988 Use of the Boltzmann equation to simulate lattice-gas automata. *Phys. Rev. Lett.* **61**, 2332.

SULSKY, D. & BRACKBILL, J. U. 1991 A numerical method for suspension flow. *J. Comput. Phys.* **96**, 339.

TRAN-CONG, T. & PHAN-THIEN, N. 1989 Stokes problems of multiparticle systems: A numerical method for arbitrary flows. *Phys. Fluids* A **1**, 453.

YEN, S. M. 1984 Numerical solution of the nonlinear Boltzmann equation for nonequilibrium gas flow problems. *Ann. Rev. Fluid Mech.* **16**, 67.

ZANETTI, G. 1989 The hydrodynamics of lattice gas automata. *Phys. Rev.* A **40**, 1539.

ZHU, J. X., DURIAN, D. J., MÜLLER, J., WEITZ, D. A. & PINE, D. J. 1992 Scaling of transient hydrodynamic interactions in concentrated suspensions. *Phys. Rev. Lett.* **68**, 2559.